Integration of Radial Turbomachinery in Small-Scale Compressed Air Energy Storage: Impact of System Size on Performance and Cost-Effectiveness

Dario Tumminello [a,CA]***, Tommaso Bacci*** [a]***, Javier Baigorri*** [b] ***and Bruno Facchini*** [a]

[a] *University of Florence, Florence, Italy*
[b] *National Renewable Energy Center (CENER), Pamplona, Spain*

Abstract:
Small-scale Compressed Air Energy Storage (CAES) systems represent a promising option for off-grid and remote energy applications, owing to their long lifetime, mechanical robustness, and limited reliance on critical raw materials. However, their performance and economic viability are strongly influenced by component technology and system scale. This study investigates the integration of radial turbomachinery in small-scale off-grid CAES systems, focusing on scaling effects, off-design operation, and system-level performance. Detailed thermodynamic models of a radial compressor and turbine are developed, incorporating performance maps, scale-dependent efficiency estimation, and variable-geometry control via inlet guide vanes (IGV) and variable stator vanes (VSV). The models are embedded in a fully integrated hybrid CAES–PV–diesel system, and a numerical optimization framework is applied to schedule IGV and VSV angles under off-design conditions and determine optimal system sizing. Results show that, at sufficiently large scales, radial turbomachinery-based CAES achieves round-trip efficiencies of approximately 50–60%, compared to 30–40% for volumetric-machine configurations. Below a critical scale, however, off-design performance degradation and higher specific costs reduce the competitiveness of turbomachinery integration. The analysis identifies a scale-dependent transition in technology suitability and provides quantitative guidelines for the application of radial turbomachinery in off-grid hybrid energy systems.

Keywords:
Compressed Air Energy Storage, Radial Turbomachinery, Turbomachinery efficiency, Techno-Economic Analysis.

1. Introduction

The increasing deployment of renewable energy sources highlights the urgent need for reliable and scalable energy storage technologies to ensure a stable electricity supply [1]. The current reliance on lithium-ion batteries raises concerns about long-term scalability, sustainability, and resilience, underscoring the need for a diversified portfolio of storage technologies [2, 3]. Among the available electrical energy storage options, Compressed Air Energy Storage (CAES) has demonstrated potential at small scales [4], especially in hybrid systems combining renewable energy, storage, and diesel generation for remote and off-grid communities [5]. The performance and economic viability of small-scale CAES systems are strongly influenced by the choice of compression and expansion technology. For the compression stage, scroll, radial, and piston compressors are available for Micro-CAES (¡1 MW [6]); piston compressors are generally preferred due to their higher achievable pressure ratios and manufacturing maturity [6, 7]. For the expansion stage, scroll expanders represent the most practical solution at low power levels, while radial turbines constitute an interesting alternative, particularly given the growing interest in micro-turbine technology [6–8]. Although the existing literature broadly addresses the selection of machine types as a function of system size, providing general guidelines in terms of flow rate and pressure ratio, direct one-to-one comparisons between competing technologies remain scarce [7, 9]. The transition to radial turbomachinery, moreover, introduces significant challenges: as machine size decreases, maintaining adequate blade tip speeds requires increasingly high rotational speeds, ultimately constrained by structural limits, while tip clearance losses become progressively dominant [10]. Power regulation under variable operating conditions introduces a further layer of complexity. Among the available control strategies for CAES compressors, Inlet Guide Vanes (IGV) regulation offers the best combination of wide operating range and efficiency retention [11]. An analogous approach based on Variable Stator Vanes (VSVs) can be applied to the expansion stage [11]. Nevertheless, only a limited number of studies have investigated the performance of IGV and VSV control in CAES operation [12]. This work addresses these gaps by developing a CAES model incorporating detailed thermodynamic representations of a radial turbomachinery, including map-based performance characterisation, scale-dependent efficiency estimation, and variable-geometry control through IGVs

and VSVs. These models are embedded within a fully integrated hybrid CAES–PV–diesel system and coupled with a numerical optimisation framework to determine optimal vane schedules under off-design conditions and identify the optimal system sizing. The results are benchmarked against a volumetric-machine baseline previously established by the same authors, with the aim of identifying the operating conditions under which radial turbomachinery provides advantages.

2. System description

The analyzed system is a stand-alone hybrid unit comprising an end-user load, a diesel generator, a photovoltaic (PV) plant, and an adiabatic micro-CAES unit. The latter consists of a four-stage centrifugal compressor, six heat exchangers, two thermal energy storage (TES) systems, a series of high-pressure vessels, a throttling valve, and a four-stage radial turbine. This configuration is derived from a layout previously analyzed by the author [13], from which it differs in two key respects: (*i*) both the compression and expansion trains employ four-stage radial turbomachinery, the additional stage being required by the lower per-stage pressure ratio achievable with centrifugal machines [9]; (*ii*) the single stratified TES is replaced by two fully mixed tanks operating at low and high temperature, respectively, to maintain an acceptable aspect ratio at larger scales. The resulting plant layout is illustrated in Figure 1. Both the compression and expansion trains are realized as four-stage integrally geared machines, in which pairs of stages are mounted on two high-speed pinion shafts driven by a central low-speed shaft connected to the motor/generator. The compressor is required to track the time-varying power output of the PV generator, while the turbine must follow the end-user load demand; power regulation strategies are therefore necessary for both machines. Since a single variable-speed drive acts on all pinion shafts simultaneously, precluding stage-wise control, inlet guide vane control is adopted for the compressor, with independently actuated vanes installed at the inlet of each stage [11, 14]. An analogous strategy is applied to the turbine via variable stator vanes, which modulate the nozzle throat area.

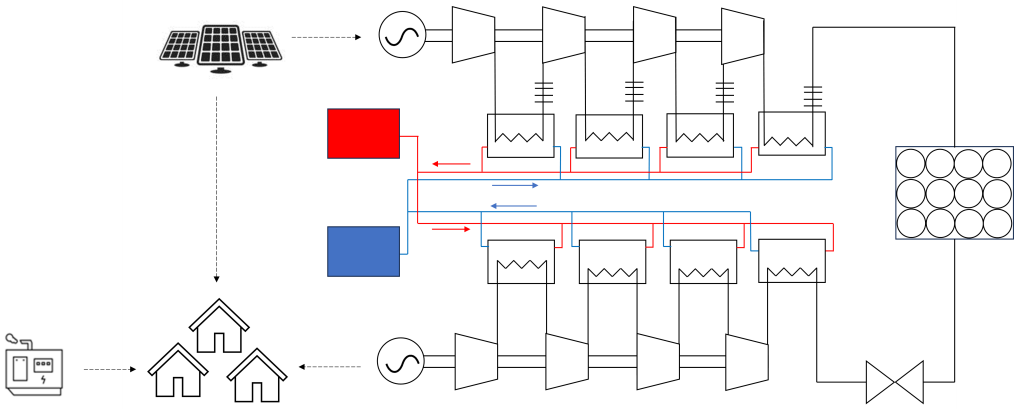

Figure 1: Plant configuration with the integration of a radial machine

3. Methodology

3.1. Energy analysis

To carry out the energy analysis, the system is implemented within the OpenModelica environment [15]. Each component is described by a system of differential–algebraic equations that capture its functional behavior, including time-dependent effects. Mass and energy conservation laws are enforced for all components. The modelling of components unchanged from the previously cited work is not described in detail here for the sake of brevity, whereas a comprehensive description of the turbomachinery models is provided in the subsequent sections. Energy performance is evaluated through the Round-Trip Efficiency (RTE) defined as the ratio between the energy released by the expander and the energy absorbed by the compressor (Equation (1)). The RTE is evaluated over an annual time horizon. To reduce computational effort, system operation is approximated using four representative weeks corresponding to different seasons, simulated sequentially with a global cyclic constraint on the storage pressure to ensure consistency with annual operation.

$$RTE = \frac{E_{ex}}{E_c} \tag{1}$$

3.2. Turbomachinery Modeling

The modeling approach adopted for turbomachinery relies on the use of performance maps. In accordance with classical turbomachinery literature, the characteristic parameters are expressed in terms of reduced (or corrected) quantities. The quantities considered are the pressure ratio (β), reduced mass flow rate ($M_r = \frac{\dot{m}\sqrt{T_1}}{p_1}$), reduced rotational speed ($N_r = \frac{N}{\sqrt{T_1}}$), and isentropic efficiency(η_{is}). Performance maps are normalized with respect to their design-point values. Henceforth, the ratio between a quantity and its corresponding design value is denoted by an overbar. The turbomachines are modeled under the assumption of adiabatic operation.

3.2.1. Compressor

To describe the compressor operating characteristics, the generalized analytical formulation proposed by Zhang and Cai [16] is employed, which is applicable to both centrifugal and axial-flow compressors. The normalized pressure ratio is expressed as a quadratic function of the reduced mass flow rate:

$$\bar{\beta} = c_1 \bar{M}_r^2 + c_2 \bar{M}_r + c_3, \tag{2}$$

while the normalized isentropic efficiency is given by

$$\bar{\eta}_{is} = \left[1 - c_4(1 - \bar{N}_r)^2\right] \frac{\bar{N}_r}{\bar{M}_r} \left(2 - \frac{\bar{N}_r}{\bar{M}_r}\right). \tag{3}$$

The coefficients c_1, c_2, and c_3 are functions of the reduced rotational speed and are defined as

$$c_1 = \frac{\bar{N}_r}{B}, \quad c_2 = \frac{p - 2q\bar{N}_r^2}{B}, \quad c_3 = -\frac{pq\bar{N}_r - m^2\bar{N}_r^3}{B}, \quad c_4 = 0.3 \tag{4}$$

where $B = p(1 - q/\bar{N}_r) + \bar{N}_r(\bar{N}_r - q)^2$. The parameters p and q depend on the compressor type. Values of $p = 1.8$ and $q = 1.8$ are typically adopted for centrifugal compressors, whereas $p = 0.36$ and $q = 1.06$ are used for axial-flow compressors. Since a centrifugal compressor is considered in this work, both p and q are set equal to 1.8.

The effect of variable inlet guide vanes on compressor performance is modeled using the correlations proposed by Haglind [17], which are widely employed in the evaluation of compressor characteristics under IGV regulation [12]. The performance parameters at a generic IGV angle are obtained from the corresponding design-angle values by applying a transformation to the reference performance maps. Let $\Delta\alpha$ denote the IGV rotation angle, while the subscript map refers to quantities evaluated at the design IGV angle. The transformed parameters are computed as

$$M_r = M_{r,\mathrm{map}} \left(1 + \frac{b_1 \Delta\alpha}{100}\right), \quad \beta - 1 = (\beta_{\mathrm{map}} - 1) \left(1 + \frac{b_2 \Delta\alpha}{100}\right), \quad \eta_{is} = \eta_{is,\mathrm{map}} \left(1 - \frac{b_3 \Delta\alpha^2}{100}\right) \tag{5}$$

The coefficients b_1, b_2, and b_3 are set to 1, 1, and 0.01, respectively. The characteristic curves obtained by applying these transformations for different values of the IGV rotation angle are shown in Figure 2 for the case of $\bar{N}_r = 1$.

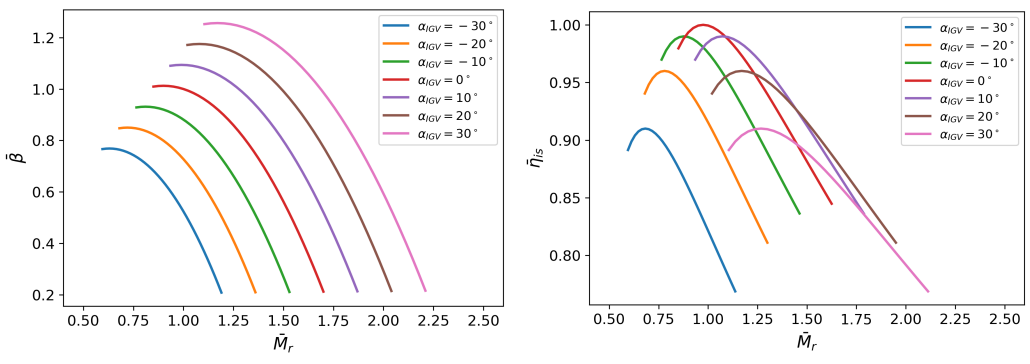

(a) (b)

Figure 2: Compressor characteristics maps under different IGV angle and $\bar{N}_r = 1$: (a) Pressure ratio, (b) Efficiency

3.2.2. Radial Turbine

Based on the same literature sources (Haglind [17]), an analytical representation of the characteristic curves of a radial turbine is also adopted. The turbine mass flow characteristics are described using a modified form of the Flügel equation:

$$\bar{M}_r = \sqrt{1.4 - 0.4\,\frac{N_t}{N_{t,n}}}\,\sqrt{\frac{1/\beta^2 - 1}{1/\beta_n^2 - 1}} \tag{6}$$

while the normalized isentropic efficiency is given by

$$\bar{\eta}_{is} = \left[1 - t_4(1 - \bar{N}_r)^2\right]\left(\frac{\bar{N}_r}{\bar{M}_r}\right)\left(2 - \frac{\bar{N}_r}{\bar{M}_r}\right) \tag{7}$$

with $t_4 = 0.3$. Using the notation previously introduced for the compressor, the effect of turbine regulation via variable stator vanes is incorporated by applying appropriate transformations to the quantities obtained from the characteristic maps corresponding to the reference case of zero VSV rotation angle. An illustrative example of these transformations is provided in Figure 3, where they are applied for the case $\bar{N}_r = 1$.

$$\frac{M_r}{M_{r,\mathrm{map}}} = 1.1875 - \frac{3}{10000}(\Delta\alpha - 25)^2, \quad \frac{\eta_{is}}{\eta_{is,\mathrm{map}}} = \left(1 - \frac{0.9}{10000}\,\Delta\alpha^2\right) \tag{8}$$

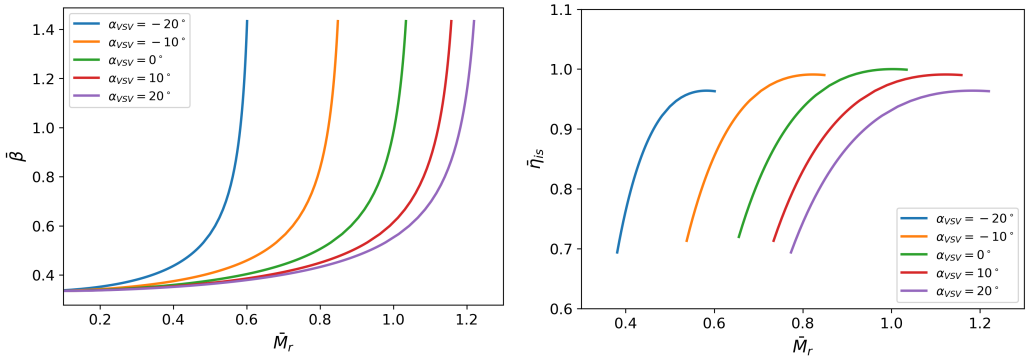

(a) (b)

Figure 3: Turbine characteristics maps under different VSV angle and $\bar{N}_r = 1$: (a) Pressure ratio, (b) Efficiency

3.3. Maximum efficiency estimation

The performance maps are scaled according to the design values of the characteristic parameters. While design mass flow rate and pressure ratio are treated as free variables, the isentropic efficiency is inherently linked to machine size and technology level. Under conventional operating conditions, well-designed stages achieve efficiencies of 85–88% for compressors and slightly higher for turbines [18]. At reduced scales, however, efficiency degrades significantly: as machine size decreases, maintaining adequate blade tip speeds requires increasing rotational speeds, ultimately constrained by mechanical limits, while tip clearance losses become progressively dominant [10, 19]. To account for these penalties while remaining grounded in standard technology, a maximum rotational speed of 50 krpm is imposed on the high-speed pinion shafts, consistent with industrially proven integrally geared machines with oil-lubricated tilted-pad bearings [20, 21] and representative of the upper boundary of conventional technology without resorting to magnetic bearings [22, 23]. Stage efficiency is estimated via the Baljé–Cordier similarity framework [19, 24], which expresses peak achievable efficiency as a function of specific speed ω_s and specific diameter D_s:

$$\omega_s = \omega \cdot \frac{\dot{V}^{1/2}}{w^{3/4}} = \frac{\Psi^{1/4}}{\Phi^{1/2}} \tag{9}$$

$$D_s = D \cdot \frac{w^{1/4}}{\dot{V}^{1/2}} = \frac{\Phi^{1/2}}{\Psi^{3/4}} \tag{10}$$

The estimation procedure is structured as follows:

1. The volumetric flow rate and isentropic specific work are derived from the design mass flow rate and pressure ratio.
2. A target specific speed is selected per Baljé criteria: $\omega_{s,\mathrm{target}} = 0.8$ for the compressor and 0.45 for the turbine.
3. The corresponding target rotational speed N_{target} is compared against N_{max}; if exceeded, the speed is capped at N_{max}.

4. The actual ω_s is computed from the effective speed, and $D_{s,\mathrm{opt}}$ is obtained from the Cordier correlation.
5. The peak stage efficiency $\eta_{\max} = f(\omega_s)$ is evaluated at $D_s = D_{s,\mathrm{opt}}$ using data from [10, 25].

The resulting efficiency values, shown in Figure 4, are further corrected for Reynolds number effects following Capata and Sciubba [26], specifically developed for small-scale radial turbomachines:

$$\frac{1-\eta}{1-\eta_{\mathrm{ref}}} = 0.50 + 0.50 \left(\frac{\mathrm{Re}_{\mathrm{ref}}}{\mathrm{Re}} \right)^{0.084 \left(\frac{\mathrm{Re}_{\mathrm{ref}}}{\mathrm{Re}} \right)^{0.25}} \tag{11}$$

where $\mathrm{Re} = uD/\nu$, with u the peripheral velocity, D the impeller diameter, and ν the kinematic viscosity. Tip clearance losses are not explicitly modeled, as their quantification would require detailed geometric information unavailable at the preliminary design level.

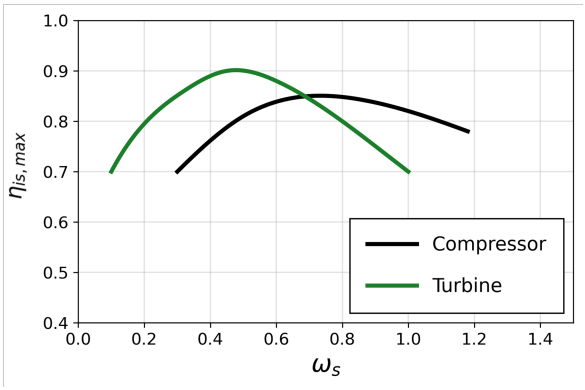

Figure 4: Maximum efficiency as a function of specific speed along the Cordier line.

3.4. Operation strategy of the hybrid model and IGV-VSV Angle Optimization

Regulation is required during both charging and discharging phases to track the instantaneous power imbalance between photovoltaic generation and load demand. The control strategy relies on inlet guide vanes (IGVs) and variable stator vanes (VSVs): a proportional–integral (PI) controller [27] modulates the first-stage vane angle α_1 within the allowable range ($-30°$ to $30°$ for the compressor, $-25°$ to $25°$ for the turbine) to match the required power via mass flow rate adjustment. The remaining vane angles α_i ($i = 2, \ldots, 4$) are scheduled as functions of α_1 and outlet/inlet pressure via look-up tables derived from a prior efficiency-maximization procedure described below.

Optimal IGV/VSV maps are generated through a genetic algortihm based optimization of the compression train model (an analogous procedure is applied to the expansion phase). A PI controller regulates α_1 to track a prescribed reduced mass flow rate, while α_2, α_3, α_4 are treated as independent decision variables. An intercooler between each stage restores air to ambient conditions ($p = 1\,\mathrm{bar}$, $T = 25\,°\mathrm{C}$); bypassing one or two final stages is also permitted at very low pressure ratios. Quasi-steady-state simulations are performed over the full operating envelope, with all quantities expressed in non-dimensional form to allow application across different design scales. For each combination of outlet pressure and reduced mass flow rate, a genetic algorithm minimizes the specific compression work by optimizing the three downstream IGV angles, yielding maps subsequently embedded in the full CAES model via look-up tables.

3.5. Economic analysis

The economic analysis is based on the evaluation of the system Levelized Cost of Energy. Equation (12) defines the LCOE as a function of the total capital expenditure (CAPEX), the annual costs (AC), and the total annual electrical energy delivered to the end user by all energy sources (E_L). The annual costs include maintenance cost as well as diesel fuel purchase costs. The investment cost of each system component is estimated using the cost functions summarized in Table 1 and updated to current values using the Chemical Engineering Plant Cost Index (CEPCI). A system lifetime of 25 years is assumed. Annual maintenance costs are taken as 2% of the total capital investment, and a discount rate of 5% is adopted, in line with values commonly used in techno-economic assessments of similar energy systems [28, 29].

$$LCOE = \frac{CAPEX + \sum_{i=1}^{Y} \frac{AC}{(1+d)^i}}{\sum_{i=1}^{Y} \frac{E_L}{(1+d)^i}} \tag{12}$$

Table 1: Cost function for main system components

Component	Capital cost estimation [$]	Year	CEPCI	
Compressor	$C = 8100 \cdot P\,(kW))^{0.6}$	2008	575	[30]
Expander	$C = 10^{\left(2.2476+1.4965\log_{10}(P)-0.1618[\log_{10}P)]^2\right)}$	2002	395.6	[31]
Heat exchanger	$C = 1096 \cdot \left(10.76 \cdot A\,(m^2)\right)^{0.18} \quad (A < 10m^2)$	2005	468.5	[32]
	$C = 8500 + 409 \cdot A^{0.85} \quad (A > 10m^2)$	2005	468.5	[33]
Air reservoir	$C = 1000 \cdot V\,(m^3) \cdot F_p$	2022	816	[34]
	$F_p = \frac{1}{0.0063} \cdot \left(\frac{(p_{\max}\,(\mathrm{bar})+1)\cdot D}{2(850-0.6(p_{\max}+1))} + 0.00315\right)$			
Thermal oil tank	$C = 423 \cdot V\,(m^3)$	2018	605.2	[35]
Thermal oil	$C = 2.7 \cdot m\,(kg)$	2018	605.2	[28]
PV system	$C = 1050 \cdot P_p\,(kW_p)$	2023	803.3	[36]
Diesel generator	$C = 630 \cdot P\,(kW)$	2017	567	[37]
Motor/Generator	$C = 60 \cdot P\,(kW)^{0.92}$	2022	816	[38]

3.6. User load demand and system location

The system supplies an end user characterized by a load profile representative of a typical domestic demand. This load profile is shown in Figure 5 as a percentage of maximum power request. The load demand is parameterized and scaled in order to perform a parametric analysis with respect to the size of the end user, which is here defined in terms of the total energy demand. The analyzed range spans from a minimum case corresponding to an energy demand of 1 MWh/day, with a peak power of approximately 50 kW, up to a system size ten times larger. In the authors' previous work, seven installation sites were analyzed, namely Romania, Cambodia, India, Belize, Jordan, Botswana, and Zimbabwe, with Zimbabwe identified as the most promising candidate [13]. Accordingly, the present study focuses exclusively on this location.

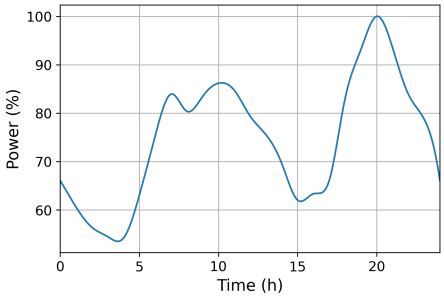

Figure 5: End user power request

3.7. Sizing optimization

A sizing procedure based on an optimization process is implemented in order to determine the optimal sizes of the various system components by coupling the thermodynamic model with the Dakota toolkit [39]. The procedure is analogous to that proposed in a previous article by the authors [40] and it is based on the use of the Efficient Global Optimization (EGO) algorithm [41]. The parameters investigated during the optimization process are summarized in Table 2, together with their corresponding exploration ranges. It should be noted that the ranges reported refer to the minimum system size considered in the parametric analysis discussed in the previous section; for the other cases, the corresponding bounds are subsequently linearly scaled in accordance with the overall system size scaling.

Table 2: Decision variables and bounds for the turbomachinery-based system sizing optimization (minimum-scale case)

Parameter	Symbol	Range
Compressor design mass flow rate	$\dot{m}_{c,n}$	0.1 ÷ 1 kg/s
Turbine design mass flow rate	$\dot{m}_{t,n}$	0.1 ÷ 1 kg/s
Pressure vessels volume	V	10 ÷ 200 m^3
Max air pressure inside vessels	p_{max}	40 ÷ 200 bar
PV installed power	PV	100 ÷ 1000 kW

4. Results

4.1. Results of IGV optimization

This section presents the results of the optimization procedure described previously. All curves are reported in non-dimensional form, with pressure levels and reduced mass flow rates normalized by their corresponding design values. Figure 6 shows the first-stage IGV angle α_1 as a function of the normalized reduced mass flow rate for six back-pressure levels, together with the optimized downstream IGV angles as functions of α_1. For the lowest back-pressure condition only α_2 is available; at the second lowest, both α_2 and α_3 are present; for the remaining four cases all three downstream angles are defined. This is a direct consequence of the bypass strategy, which excludes the final stages under low back-pressure conditions. As shown in Figure 6-(a), α_1 varies nearly linearly with $\bar{M}_r$, consistent with the modulation of the effective flow area under fixed inlet density conditions, as expressed in Equation (5). The downstream IGV angles (Figure 6-(b)–(d)) exhibit significantly smaller variation ranges; the third stage shows the smallest. The angles of the first three stages increase with $\bar{M}_r$ at progressively decreasing rates, while the fourth-stage angle follows the opposite trend and displays a markedly stronger dependence on the total compression ratio.

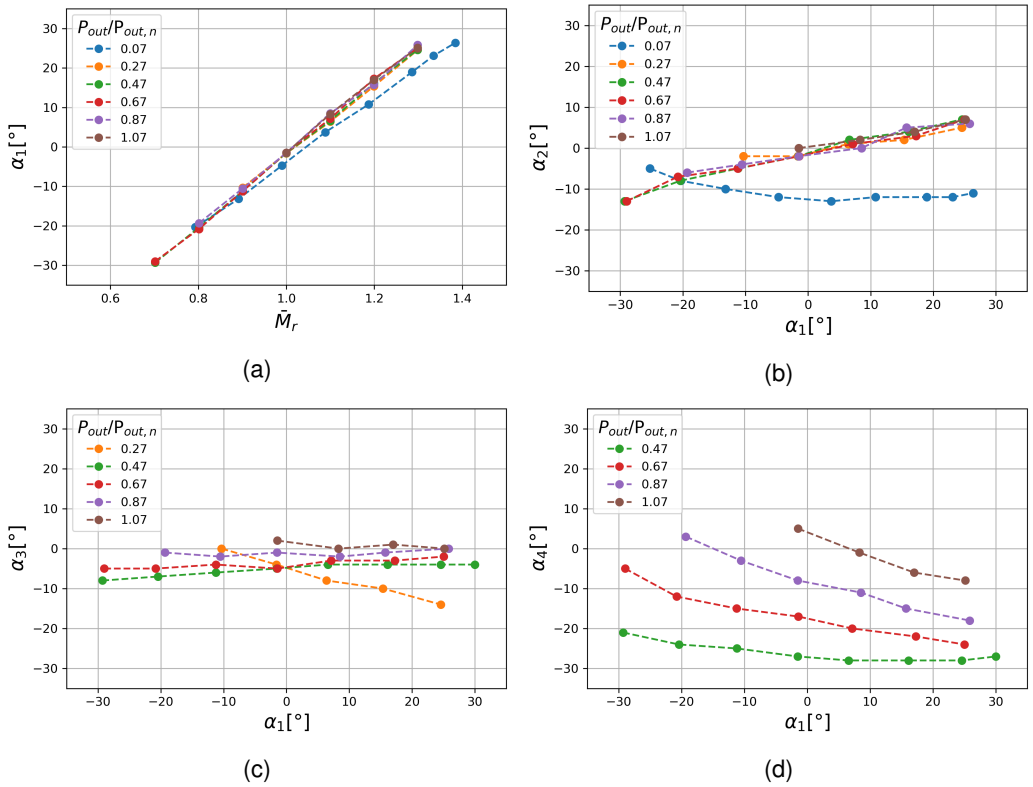

Figure 6: Optimized IGV angles for different back-pressure levels.

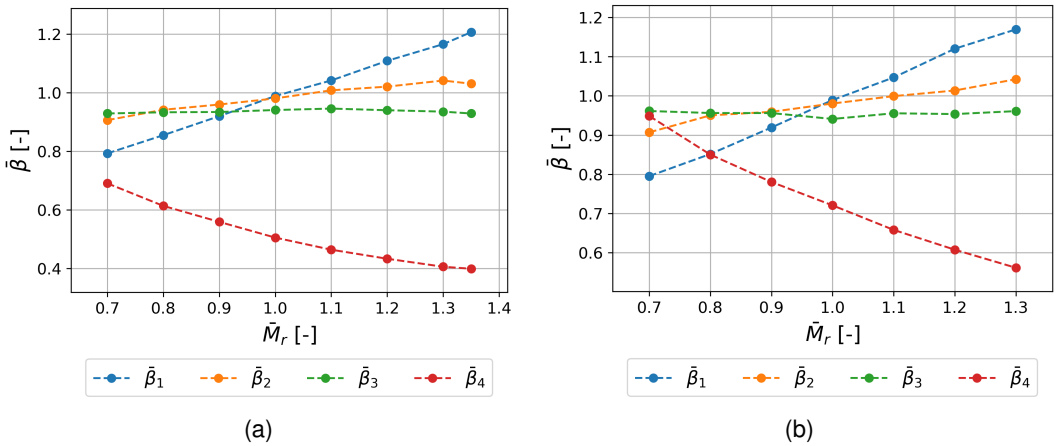

Figure 7: Normalized pressure coefficient $\bar{\beta}$ vs. normalized reduced mass flow rate for four compression stages: (a) $P_{\text{out}}/P_{\text{out,n}} = 0.47$, (b) $P_{\text{out}}/P_{\text{out,n}} = 0.67$.

At outlet pressures of $P_{out}/P_{\mathrm{out,n}} = 0.07$ and $P_{out}/P_{\mathrm{out,n}} = 0.27\,P_{\mathrm{out,n}}$, the trends of α_2 and α_3 resemble that of α_4 in the other conditions, since in those cases the second and third stages act as the final active compression stage. These trends reflect the underlying optimization strategy, which can be interpreted through the pressure ratio distribution among the stages. The IGV angles of the first three stages are adjusted to maintain operation close to their respective design points, thereby maximizing their isentropic efficiencies. The fourth stage, in contrast, primarily serves to satisfy the required back-pressure constraint and is therefore allowed to operate further from its design point. As a consequence, it exhibits the lowest isentropic efficiency among all stages and, operating under off-design conditions, is also characterized by a reduced pressure coefficient $\bar{\beta}$, implying that it absorbs less work than the upstream stages. This behavior is confirmed by Figure 7, which reports $\bar{\beta}$ for each compression stage at two outlet pressure levels as a function of the first-stage reduced mass flow rate $\bar{M}_{r,1}$. As $\bar{M}_{r,1}$ increases, the pressure coefficient of the first stage increases accordingly, while those of the second and third stages remain nearly constant and close to unity, indicating sustained near-design operation. The fourth stage exhibits the opposite trend, with $\bar{\beta}$ departing progressively from unity as the mass flow rate increases, confirming that it operates furthest from its optimal design point.

The optimization results for the turbine are reported in Figure 8, which refer to operating conditions in which all four expansion stages are active. Results for configurations in which the first stage is bypassed are omitted for sake of brevity.

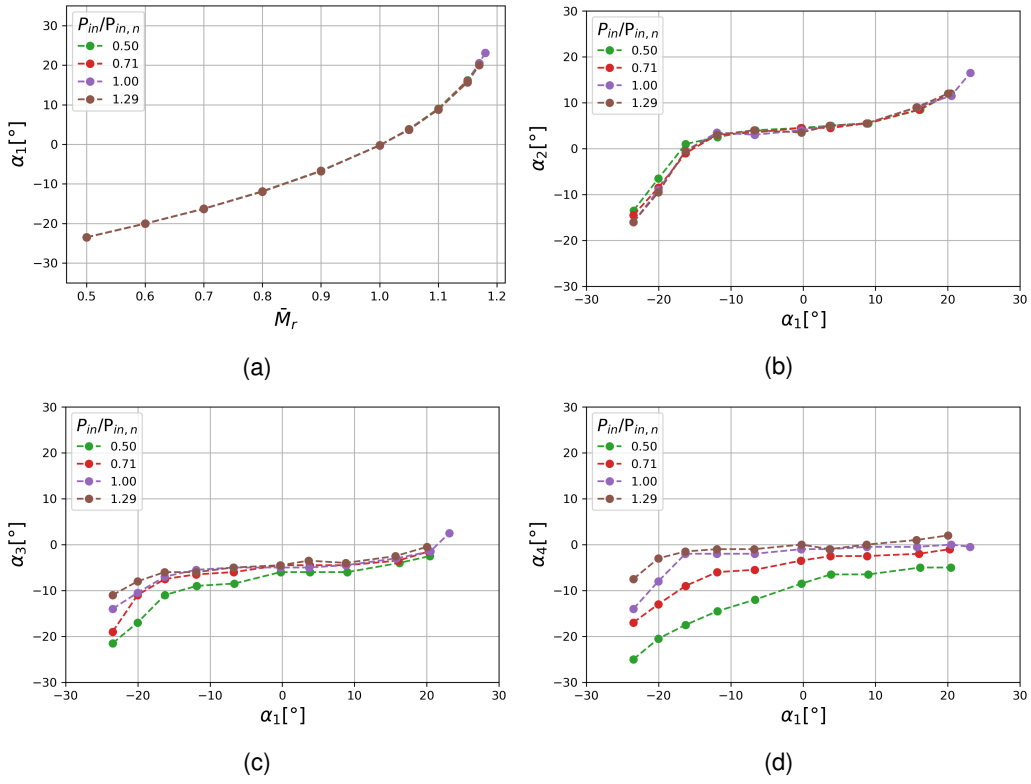

Figure 8: Optimized VSV angles for different inlet pressure levels.

As shown in Figure 8-(a), the first-stage VSV angle increases with $\bar{M}_r$, since a wider nozzle opening is required to sustain the prescribed expansion ratio at higher mass flow rates. Unlike the compressor, where mass flow rate responds approximately linearly to IGV deflection, the turbine exhibits a quadratic dependence, as expressed by Equation (8), which is clearly reflected in the shape of the curves. The downstream VSV angles (Figure 8-(b)–(d)) increase with α_1 before stabilizing near $0°$, with inlet pressure having a limited influence except on the last stage. The underlying mechanism is clarified by the expansion ratio distributions in Figure 9. At moderate inlet pressures (Figure 9-(a)), the first stage delivers the highest expansion ratio, which remains approximately constant at 1.4 for low VSV angles and decreases as α_1 increases. This is consistent with the shift of the peak-efficiency point toward lower expansion ratios under VSV regulation; the downstream angles are simultaneously adjusted to prevent choking and keep the first stage near its optimal operating point. At higher inlet pressures Figure 9-(b)), a different regime emerges: the fourth-stage expansion ratio rises substantially, eventually exceeding that of the first stage. This redistribution reflects the optimizer's preference for keeping the last-stage VSV angle near $0°$: since large VSV deflections impose a greater efficiency penalty than a suboptimal expansion ratio distribution, and since the last stage contributes a significant share of the total turbine work, it is preferable to accept the latter rather than incur the former.

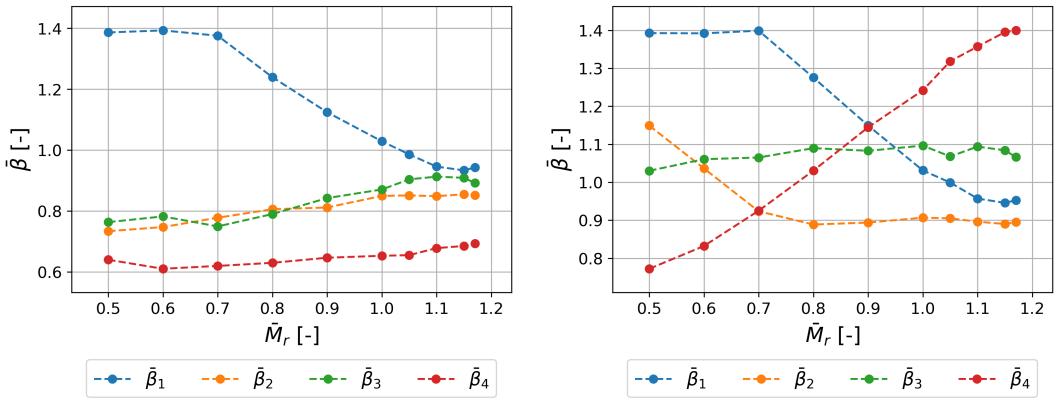

(a) (b)

Figure 9: Normalized expansion ratio vs. normalized reduced mass flow rate for four turbine stages: (a) $P_{\text{in}}/P_{\text{in,n}} = 0.50$, (b) $P_{\text{in}}/P_{\text{in,n}} = 1.28$.

4.2. Result of case study

The results for the case study are presented in Figure 10, which reports the levelized cost of energy of the hybrid system as a function of daily energy demand. The figure also includes the LCOE previously obtained for the configuration employing volumetric machines, as well cases in which the demand is met solely by a diesel generator, or by a diesel generator coupled with photovoltaics without storage. The LCOE trend for the hybrid system based on radial turbomachinery exhibits an approximately hyperbolic behavior, with a maximum value of 0.29$/kWh at 1 MWh/day. The LCOE decreases rapidly up to about 3 MWh/day and more gradually thereafter, reaching 0.202 $/kWh at 10 MWh/day. A comparison with the volumetric-machine configuration reveals a crossover at approximately 3 MWh/day: below this threshold, volumetric machines yield lower LCOE, whereas turbomachinery becomes economically preferable at larger scales. This behavior highlights a clear technological trade-off. The crossover corresponds to a CAES system characterized by a compressor rated at approximately 400 kW, a turbine at about 150 kW, and a storage capacity of roughly 1.4 MWh. Both configurations exhibit lower LCOE values compared to systems without storage, demonstrating that the integration of energy storage is economically advantageous. The figure also reports the round-trip efficiency of the optimized configurations. Unlike the volumetric-machine case, where RTE remained nearly constant at 35%, the turbomachinery-based system exhibits a marked scale dependence, rising from 41% at 1 MWh/day to 54% at 10 MWh/day. At small scales, however, this efficiency advantage is insufficient to offset the higher capital costs associated with the more complex turbomachinery solution, so that the overall economic performance remains less favorable than that of the volumetric configuration. The RTE trend is primarily driven by the scale dependence of stage isentropic efficiency, as discussed in Section 3.3.. This degradation stems from the 50 krpm rotational speed limit imposed on the high-speed pinion shafts, which prevents small machines from operating at the optimal specific speed. The stage efficiencies for both the compression and expansion trains are reported in Figure 11 as a function of machine power. For the compressor, stage efficiencies de-

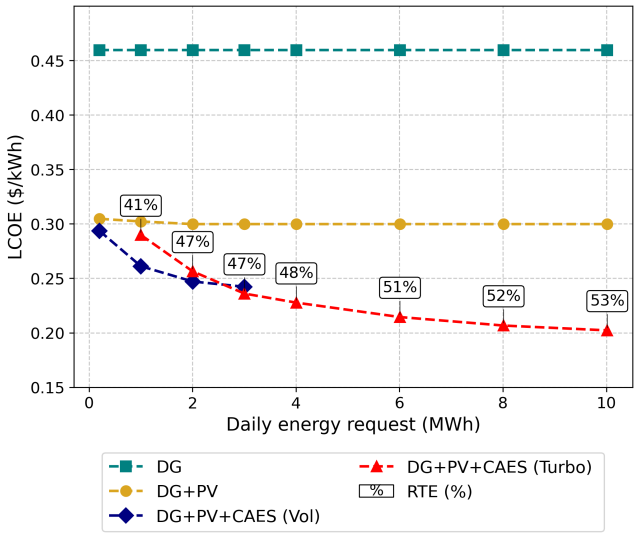

Figure 10: LCOE of the hybrid system at different system scales.

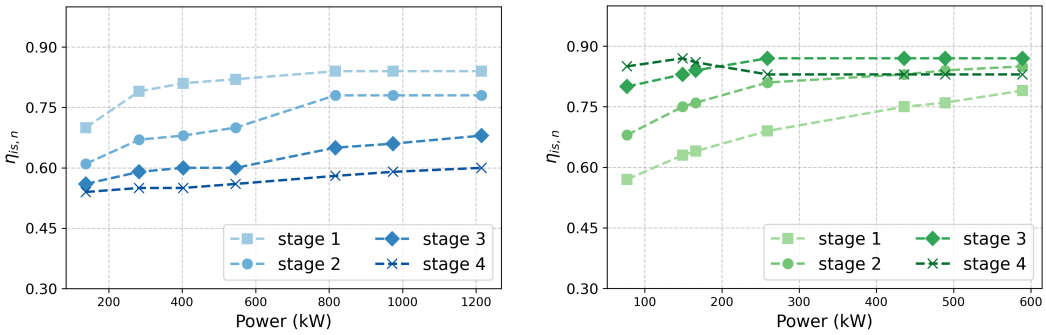

(a) (b)

Figure 11: Maximum isentropic efficiency of machine stages: (a) compressor, (b) turbine.

crease progressively from the first to the fourth stage, owing to the reduction in volumetric flow rate — and thus specific speed ω_s — along the compression path. All stages improve with increasing machine size, as higher volumetric flow rates shift ω_s toward its optimum value.Beyond a critical size, the first and second stages saturate: they can already achieve the target $\omega_s = 0.8$ at rotational speeds below the imposed limit, so that further scaling leaves their efficiency unchanged. The third and fourth stages do not exhibit this plateau, as the lower volumetric flow rates associated with higher compression pressures would require even greater rotational speeds to reach the same specific speed. Analogous considerations apply to the turbine (Figure 11-(b)): when the speed constraint is active, downstream expansion stages benefit from larger volumetric flow rates and thus operate closer to their optimal conditions. Once the optimal specific speed is attained on the first stage of a given shaft, that stage exhibits the highest efficiency, while the subsequent stage operates slightly off its design point, as clearly visible for the shaft carrying the third and fourth expansion stages.

The main design parameters and performance indicators of the optimized configurations are summarized in Table 3. The optimal storage pressure increases with system size, converging to a plateau of approximately 175 bar. At small scales, the rotational speed constraint forces a reduction in stage pressure ratio to keep ω_s near its optimum, resulting in lower operating pressures. As machine size increases and this constraint becomes less binding, the optimal pressure is governed primarily by storage economics: the vessel cost function exhibits a minimum in the 160–180 bar range, within which costs are minimized and show limited sensitivity to pressure. This behavior contrasts with the volumetric-machine case, where the optimal pressure (117 bar) was limited by the effect of back-pressure on compressor volumetric efficiency — specifically, higher discharge pressures increase the clearance volume, reducing the effective air delivery during charging.

Table 3: Optimized configurations for Zimbabwe at different system sizes.

E_L [MWh/day]	V [m^3]	$\dot{m}_{c,n}$ [kg/s]	$\dot{m}_{t,n}$ [kg/s]	p_{max} [bar]	PV [kW]	RTE [%]	LCOE [$/kWh]
1	67.3	0.19	0.23	92	389	41.5	0.290
2	124.5	0.40	0.43	101	749	46.7	0.256
3	124.0	0.54	0.47	136	1077	47.2	0.236
4	126.5	0.70	0.72	170	1440	47.8	0.228
6	180.0	1.04	0.95	173	2061	50.5	0.214
8	235.1	1.39	1.20	176	2683	52.1	0.207
10	287.0	1.69	1.38	175	3251	53.2	0.202

5. Conclusions

This study investigated the scalability of hybrid PV-diesel-CAES systems employing radial turbomachinery in the compression and expansion stages, with the aim of assessing the energetic and economic performance improvements over volumetric-machine-based configurations. A map-based turbomachinery performance model, incorporating scale-dependent efficiency ceilings and off-design control schedules via inlet and variable stator vanes, was developed and embedded in a full plant model for system-level optimization. The results show that the LCOE decreases monotonically with system scale, from approximately 0.29 $/kWh at small sizes to 0.20 $/kWh at 10 MWh/day, following a near-hyperbolic trend. A crossover point between turbomachinery- and volumetric-based configurations is identified at around 3 MWh/day: below this threshold, volumetric machines remain economically preferable, while radial turbomachinery becomes the cost-effective choice at larger scales. This behavior is closely linked to the scale dependence of isentropic efficiency, which drives the round-trip efficiency from 41% at small scales up to 54% at larger ones, a trend absent in volumetric systems. At

small scales, performance is further penalized by rotational speed constraints that prevent operation at optimal specific speed conditions. The optimal storage pressure increases with system size, converging toward 175 bar, consistent with the minimum of the pressure vessel cost curve. These findings highlight that neglecting turbomachinery efficiency degradation at small scales leads to overly optimistic performance estimates, and provide practical design guidelines for CAES system studies.

References

[1] David Mohler and Daniel Sowder. Energy storage and the need for flexibility on the grid. In *Renewable energy integration*, pages 309–316. Elsevier, 2017.

[2] Ben Bin Xu, Yinzhu Jiang, Terence Xiaoteng Liu, Zaiping Guo, Guihua Yu, and Maria-Magdalena Titirici. Beyond lithium: a new era of sustainable energy engineering, 2022.

[3] Yifei Deng, Yijing Wang, Xiaofan Xing, Yuankang Xiong, Siqing Xu, and Rong Wang. Requirement on the capacity of energy storage to meet the 2° c goal. *Sustainability*, 16(9):3753, 2024.

[4] *Concept and Application of Distributed Compressed Air Energy Storage Systems Integrated in Utility Networks*, ASME Power Conference, 07 2013. doi: 10.1115/POWER2013-98113.

[5] Hussein Ibrahim and Adrian Ilinca. Contribution of the compressed air energy storage in the reduction of ghg-case study: Application on the remote area power supply system. In *Air Pollution-A Comprehensive Perspective*. IntechOpen, 2012.

[6] Yanlin Zheng, Huan Guo, Hualiang Zhang, Wenbin Guo, Mingzhi Zhao, Yujie Xu, Jingjian Huang, and Haisheng Chen. A review of micro compressed air energy storage: Applications, component selection, and dynamic modeling. *Journal of Energy Storage*, 137:118614, 2025.

[7] Wei He and Jihong Wang. Optimal selection of air expansion machine in compressed air energy storage: A review. *Renewable and Sustainable Energy Reviews*, 87:77–95, 2018.

[8] Hao Sun, Xing Luo, and Jihong Wang. Feasibility study of a hybrid wind turbine system–integration with compressed air energy storage. *Applied Energy*, 137:617–628, 2015.

[9] Royce N Brown. *Compressors: Selection and sizing*. Gulf Professional Publishing, 1997.

[10] Marco Gambini and Michela Vellini. *Turbomachinery: fundamentals, selection and preliminary design*. Springer Nature, 2020.

[11] Huan Guo, Yujie Xu, Haoyuan Kang, Wenbing Guo, Yu Liu, Xinjing Zhang, Xuezhi Zhou, and Haisheng Chen. From theory to practice: Evaluating the thermodynamic design landscape of compressed air energy storage systems. *Applied Energy*, 352:121858, 2023.

[12] Huan Guo, Yujie Xu, Yi Zhang, Qi Liang, Hongtao Tang, Xinjing Zhang, Zhitao Zuo, and Haisheng Chen. Off-design performance and an optimal operation strategy for the multistage compression process in adiabatic compressed air energy storage systems. *Applied Thermal Engineering*, 149:262–274, 2019.

[13] Dario Tumminello, Claudio Zuffi, Tommaso Bacci, and Bruno Facchini. Hybrid micro-compressed air energy storage with photovoltaic and diesel generation for off-grid applications: A parametric life cycle and techno-economic study. *Cleaner Energy Systems*, page 100246, 2026. ISSN 2772-7831. doi: https://doi.org/10.1016/j.cles.2026.100246.

[14] H Simon, T Wallmann, et al. Improvements in performance characteristics of single-stage and multistage centrifugal compressors by simultaneous adjustments of inlet guide vanes and diffuser vanes. *Journal of turbomachinery*, 109(1):41–47, 1987.

[15] Peter Fritzson, Peter Aronsson, Håkan Lundvall, Kaj Nyström, Adrian Pop, Levon Saldamli, and David Broman. The openmodelica modeling, simulation, and software development environment. *Simulation News Europe*, 44:8–16, 2005.

[16] Na Zhang and Ruixian Cai. Analytical solutions and typical characteristics of part-load performances of single shaft gas turbine and its cogeneration. *Energy Conversion and Management*, 43(9-12):1323–1337, 2002.

[17] Fredrik Haglind. Variable geometry gas turbines for improving the part-load performance of marine combined cycles–gas turbine performance. *Energy*, 35(2):562–570, 2010.

[18] S Larry Dixon and Cesare Hall. *Fluid mechanics and thermodynamics of turbomachinery*. Butterworth-Heinemann, 2013.

[19] OE Balje. A study on design criteria and matching of turbomachines: Part a — similarity relations and design criteria of turbines. 1962.

[20] MAN Energy Solutions. Integrally geared compressors. Web page. URL `https://www.man-es.com/`

process-industry/products/compressors/integrally-geared-compressors/energy-and-storage/energy-storage-laes.

[21] Atlas Copco Gas and Process Solutions. *Driving Centrifugal Compressor Technology*, n.d. URL https://www.atlascopco.com/content/dam/atlas-copco/compressor-technique/gas-and-process/documents/driving-centrifugal-compressor-technology-new.pdf. Brochure, 19+ pp.

[22] Andreas P Weiss and Gerd Zinn. Micro turbine generators for waste heat recovery and compressed air energy storage. In *Proc. 15th Conf. on Power System Engineering, Thermodynamics & Fluid Flow: ES*, pages 978–80, 2016.

[23] An Sung Lee and Bum Seog Choi. Evaluation of foii bearing performance and noniinear rotordynamics of 120 kw oii-free gas turbine generator. 2014.

[24] Otto Cordier. Ähnlichkeitsbedingungen für strömungsmaschinen. *BWK Bd*, 6(10):337–340, 1953.

[25] Colin Rodgers. The efficiencies of single-stage centrifugal compressors for aircraft applications. In *Turbo Expo: Power for Land, Sea, and Air*, volume 78989, page V001T01A025. American Society of Mechanical Engineers, 1991.

[26] Roberto Capata and Enrico Sciubba. Use of modified balje maps in the design of low reynolds number turbocompressors. In *ASME International Mechanical Engineering Congress and Exposition*, volume 45233, pages 835–841. American Society of Mechanical Engineers, 2012.

[27] Kok K Tan, Qing-Guo Wang, and Chang C Hang. *Advances in PID control*. Springer Science & Business Media, 2012.

[28] Sike Wu, Cheng Zhou, Elham Doroodchi, and Behdad Moghtaderi. Techno-economic analysis of an integrated liquid air and thermochemical energy storage system. *Energy Conversion and Management*, 205:112341, 2020.

[29] Da Li and Liqiang Duan. Techno-economic analysis of solar aided liquid air energy storage system with a new air compression heat utilization method. *Energy Conversion and Management*, 278:116729, 2023.

[30] Mathieu Legrand, Raúl Labajo-Hurtado, Luis Miguel Rodríguez-Antón, and Yolanda Doce. Price arbitrage optimization of a photovoltaic power plant with liquid air energy storage. implementation to the spanish case. *Energy*, 239:121957, 2022.

[31] Richard Turton, Richard C Bailie, Wallace B Whiting, and Joseph A Shaeiwitz. *Analysis, synthesis and design of chemical processes*. Pearson Education, 2008.

[32] James R Couper. *Chemical process equipment: selection and design*. Gulf professional publishing, 2005.

[33] Ibrahim Din, Marc A Rosen, Pouria Ahmadi, et al. *Optimization of energy systems*. John Wiley & Sons, 2017.

[34] Mohamad Cheayb, Mylène Marin Gallego, Mohand Tazerout, and Sébastien Poncet. A techno-economic analysis of small-scale trigenerative compressed air energy storage system. *Energy*, 239, 1 2022. ISSN 03605442.

[35] Haobai Xue and Alexander White. A comparative study of liquid, solid and hybrid adiabatic compressed air energy storage systems. *Journal of Energy Storage*, 18:349–359, 2018.

[36] Lazard's levelized cost of energy analysis—version 16.0, 2023. URL https://www.lazard.com/media/typdgxmm/lazards-lcoeplus-april-2023.pdf.

[37] K. Gnana. Lazard's levelized cost of energy analysis—version 11.0. Report, Lazard, 2017. URL https://www.lazard.com/perspective/levelized-cost-of-energy-2017/.

[38] Peng Li, Qingya Hu, Guoneng Li, Binbin Wang, Yaping Bai, Xu Han, and Zhonghe Han. Research on thermo-economic characteristics of a combined cooling, heating and power system based on advanced adiabatic compressed air energy storage. *Journal of Energy Storage*, 47:103590, 2022.

[39] Brian M Adams, William J Bohnhoff, Keith R Dalbey, Mohamed S Ebeida, John P Eddy, Michael S Eldred, Russell W Hooper, Patricia D Hough, Kenneth T Hu, John D Jakeman, et al. Dakota, a multilevel parallel object-oriented framework for design optimization, parameter estimation, uncertainty quantification, and sensitivity analysis: version 6.13 user's manual. Technical report, Sandia National Lab.(SNL-NM), Albuquerque, NM (United States), 2020.

[40] Dario Tumminello, Tommaso Bacci, Bruno Facchini, et al. Numerical modeling and design optimization of a micro-caes system. In *37th International Conference on Efficiency, Cost, Optimization, Simulation and Environmental Impact of Energy Systems, ECOS 2024*, volume 1, pages 24–35. ECOS 2024, 2024.

[41] Donald R Jones, Matthias Schonlau, and William J Welch. Efficient global optimization of expensive black-box functions, 1998.